

Spectral imaging facilitates visualization and measurements of unstable and abnormal microvascular oxygen transport in tumors

Brian S. Sorg*

University of Florida
J. Crayton Pruitt Family Department of Biomedical
Engineering
130 BME Building
Gainesville, Florida 32611-6131
and
Duke University Medical Center
Department of Radiation Oncology
Durham, North Carolina 27705

Matthew E. Hardee

Duke University Medical Center
Department of Radiation Oncology
Durham, North Carolina 27705

Nikita Agarwal

University of Florida
J. Crayton Pruitt Family Department of Biomedical
Engineering
130 BME Building
Gainesville, Florida 32611-6131

Benjamin J. Moeller

Mark W. Dewhirst
Duke University Medical Center
Department of Radiation Oncology
Durham, North Carolina 27705

Abstract. Abnormal microvasculature contributes to the pathophysiologic microenvironment of tumors. Understanding microvascular tumor oxygen transport is necessary to comprehend the factors that influence tumor biology, physiology, and therapy. Previously, we described an *in vivo* spectral imaging microscopy system for measurements of microvessel hemoglobin saturation (HbSat). We measure temporal fluctuations and spatial gradients in tumor microvessel oxygenation and identify instances of anastomoses between vessels with significantly different oxygenations. Slow periodic fluctuations in HbSat <0.2 cycles per minute were observed. These measurements are consistent with microelectrode measurements of fluctuating tumor oxygenation. Gradients in HbSat along individual tumor microvessels were measured that were larger in magnitude than normal tissue microvessels. Images were captured of anastomoses of tumor microvessels with diameters $\leq 100 \mu\text{m}$ and significantly different HbSat values (>20%). Shunting of inspired oxygen, presumably due to arteriovenous anastomoses, from tumor feeding arterioles to adjacent venules was imaged. This effect was confined to a region around the tumor and was not observed in nearby normal microvessels. Imaging measurements of tumor microvessel oxygen transport may offer insight to current questions regarding oxygen-related tumor biology and treatment responses, and spectral imaging may be a useful research tool in this regard. © 2008 Society of Photo-Optical Instrumentation Engineers. [DOI: 10.1117/1.2837439]

Keywords: cancer; fluctuations; hemoglobin saturation; hypoxia; *in vivo* microscopy; microvasculature; oxygen; tumor; window chamber.

Paper 07185RR received May 24, 2007; revised manuscript received Sep. 25, 2007; accepted for publication Sep. 30, 2007; published online Feb. 28, 2008. This paper is a revision of a paper presented at the SPIE conference on Imaging, Manipulation, and Analysis of Biomolecules, Cells, and Tissues IV, Jan. 2006, San Jose, California. The paper presented there appears (unrefereed) in SPIE Proceedings Vol. 6088.

1 Introduction

Abnormalities in tumor microvasculature structure and function contribute to the pathophysiologic microenvironment of tumors, which is characterized by inadequate oxygen delivery for the metabolic demands of the tissue.¹⁻⁶ It is well established that hypoxia can influence tumor biology and physiology, gene expression, metastatic potential, treatment efficacy, and patient survival. In addition to the detrimental effect on radiosensitivity,⁷ hypoxia can have a direct and indirect negative impact on chemotherapy.⁸ Hypoxia not only affects cancer therapy, it also affects tumor development, and strong evidence suggests that hypoxia can drive malignant progression through gene expression.^{9,10} Given that most human solid tumors have been shown to have hypoxic regions, there is a

strong motivation to better understand the causes and consequences of tumor hypoxia.

Classically, tumor hypoxia with microvascular origins has been described as being “chronic” or “acute.” Chronic hypoxia is attributed to sparsely vascularized regions with long oxygen diffusion distances between vessels, and acute hypoxia is attributed to transient cessation of blood flow in microvessels.⁷ Recent research has added depth and complexity to the notions of chronic and acute hypoxia with the identification of other contributing factors. Two such factors are temporal fluctuations in tissue pO₂ and microvascular longitudinal gradients in oxygen transport. Prior studies have shown the existence of temporal and spatial heterogeneities in oxygenation and hypoxia in tumors using oxygen microelectrodes¹¹ and phosphorescence lifetime imaging.¹² Other research has shown the existence of low frequency (<2 cycles per minute [cpm]) fluctuations in tumor pO₂ that can lead to intermittent hypoxia without cessation of blood

*Current address: P.O. Box 116131, University of Florida, Gainesville, FL 32611-6131; Tel: 352-273-5876; Fax: 352-392-9791; E-mail: brian.sorg@bme.ufl.edu
Address all correspondence to Mark W. Dewhirst, Duke University Medical Center, MSRB 201, Box 3455, Durham, NC 27710; Tel: 919-684-4180; Fax: 919-684-8718; E-mail: dewhirst@radonc.duke.edu

flow.¹³ Recent research suggests that intermittent hypoxia may have more clinical relevance in terms of its impact on treatment and tumor progression than classically described chronic and acute hypoxia^{14–16} and thus warrants further study.

Another notable characteristic of tumor microvasculature is the existence of arteriovenous (AV) anastomoses.¹⁷ AV anastomoses are also found in some normal tissues with highly variable blood flow, such as skin.¹⁸ In tumors, however, a large portion of the blood flow, 30% in malignant tumors by some estimates,¹⁹ can be via AV shunts.²⁰ Some tumors tend to develop AV anastomoses with other organs, such as hepatocellular carcinomas, which commonly develop shunts to the lungs.²¹ An important consequence of this development is that chemotherapeutic agents can bypass the tumor,²² rendering them ineffective.

Imaging measurements of microvessel oxygen transport and function can potentially provide insight into the connections between microregional hypoxia and gene expression and may also elucidate oxygen transport effects of certain classes of drugs, such as vascular targeting agents. Previously, we described a microscope-based spectral imaging system to measure hemoglobin saturation (HbSat) in the microvasculature of tumors grown in mouse dorsal skin-fold window chambers.²³ In this paper, we demonstrate the ability of the system to measure fluctuations in tumor microvascular oxygen transport, identify connections between microvessels of very different HbSats, and document an effect on oxygen transport presumably due to tumor AV anastomoses at the microvascular level in a mouse mammary adenocarcinoma.

2 Materials and Methods

Details about the imaging system, image acquisition, and image processing methods were discussed previously^{23,24} and will be reviewed briefly below.

2.1 Imaging System

Zeiss Axioskop II (Duke University) and AxioImager (University of Florida) microscopes (Carl Zeiss, Inc., Thornwood, New York) served as the imaging platform. A 100-W tungsten halogen lamp was used for transillumination of the window chamber. Images were acquired at 1388×1024 pixels and 12-bit dynamic range with a DVC 1412 charge-coupled device (CCD) camera (DVC Company, Austin, Texas) that was thermoelectrically cooled to -20°C . The objectives used were all air immersion with long working distances (WD) (Carl Zeiss, Inc.): $2.5\times$ [numerical aperture (NA)=0.12, WD=6.3 mm] and $5\times$ (NA=0.25, WD=12.5 mm) Fluars, and a $10\times$ (NA=0.3, WD=5.5 mm) Plan-NeoFluar. Band-limited optical filtering for hyperspectral imaging was accomplished with a C-mounted liquid crystal tunable filter (CRI, Inc., Woburn, Massachusetts) with a 400- to 720-nm transmission range and 10-nm nominal bandwidth placed in front of the camera. Images were saved as 16-bit tagged image files. The field-of-view captured by the CCD camera was different for the two microscope systems due to slight demagnification ($\sim 0.75\times$, Duke microscope) or magnification ($\sim 1.5\times$, University of Florida microscope) in relay lenses used to create an infinity space for the liquid crystal tunable filter. Thus, the fields-of-view imaged by the CCD camera were the following: $2.5\times = 3.6 \times 4.9$ mm (Duke) or

2.3×3.1 mm (Florida), $5\times = 1.8 \times 2.5$ mm (Duke) or 1.2×1.6 mm (Florida), $10\times = 0.9 \times 1.2$ mm (Duke) or 0.6×0.8 mm (Florida). Scale bars in the figures give an indication of the field-of-view and object dimensions in the images.

2.2 Image Acquisition

Custom designed software created with LABVIEW (National Instruments Corp., Austin, Texas) was used to control the tuning of the filter and operation of the camera. The software allows automated image acquisition with user-specified camera exposure time and gain for each filter wavelength. For each HbSat time point, 16 images were acquired from 500 to 575 nm in 5-nm intervals. The transmission of the liquid crystal tunable filter is lower at shorter wavelengths and higher at longer wavelengths; therefore, the image acquisition time was adjusted *a priori* for each wavelength such that the full dynamic range of the camera was used. The minimum exposure time used was 300 ms to average out fluctuations in the signal due to random red blood cell motion.²³ A typical data set was acquired in about 13 s, which included image acquisition, filter tuning, image transfer, and saving of the images to the computer hard drive.

2.3 In vivo Surgery and Imaging

All *in vivo* experiments were conducted under protocols approved by the Duke University Institutional Animal Care and Use Committee and the University of Florida Institutional Animal Care and Use Committee. A titanium window chamber was surgically implanted under anesthesia [ketamine 100 mg/kg intraperitoneal (IP) and xylazine 10 mg/kg IP] on the back of athymic (nu/nu) nude mice. The tumors used in these experiments were the 4T1 metastatic mouse mammary adenocarcinoma and the 4TO7 nonmetastatic subclone of the 4T1 tumor. A window chamber tumor was established during chamber implantation by injecting $10\ \mu\text{L}$ of a single cell suspension of 5×10^3 cells into the dorsal skin flap prior to placing a 12-mm diameter #2 round glass coverslip (Erie Scientific, Portsmouth, New Hampshire) over the exposed skin. In this window chamber model, one piece of skin was removed completely and replaced with a coverslip, but the other piece of skin in the window chamber remained intact and without any coverslip. The tumor had unrestricted growth on the side of the chamber without a coverslip and thus bulged out during growth. This limited transillumination imaging to a maximal tumor size of about 2 to 3 mm because the light that penetrated the tumor was insufficient for the hyperspectral imaging technique due to poor signal to noise ratio and experiments were terminated at this point. Animals were housed in an environmental chamber with free access to food and water and standard 12-h light and dark cycles. Animals were placed on a heating pad attached to the microscope stage during the imaging session. A custom-built window chamber holder secured the window chamber under the microscope objective. The holder was fastened to a stage mount that allowed the window chamber to be positioned under the microscope objective using the standard manual controls on the microscope stage. Anesthesia for immobilization during imaging was provided by isoflurane (1 to 1.5%) in medical air. Image data sets were acquired as follows. (1) For investigations of time-

averaged values of HbSat in microvessels, image data sets were acquired at intervals of 1 or 3 min for approximately 1 h. (2) For HbSat fluctuation analysis, image data sets were acquired at 20-s intervals for 40 min. Data set acquisition at 20-s intervals represents the maximum achievable time resolution with the current imaging system parameters, with image exposure time being the limiting factor. In one set of experiments, animals were imaged while the breathing gases were changed from room air to 100% oxygen. In this case, anesthesia for immobilization during imaging was provided by ketamine 100 mg/kg IP and xylazine 10 mg/kg IP.

2.4 Image and Data Processing

Image processing was performed using MATLAB software (The Mathworks, Inc., Natick, Massachusetts). All images were converted into double-precision arrays for mathematical processing. The raw pixel values were converted to absorbance values by manually selecting avascular regions in the images to use as an estimate of unattenuated light. Pure reference spectra of oxy- and deoxyhemoglobin obtained with the imaging system were used in a linear mixing model to solve for HbSat by a linear least-squares regression of the data according to the method of Shonat²⁵ as described previously.^{23,24} Regions-of-interest (ROIs) on individual microvessels were manually selected for data points of HbSat. The calculated values of HbSat for each pixel were accepted or rejected based on the R^2 value for the fit of the model to the data based on the calculated unknowns. R^2 was calculated according to the standard definition for the coefficient of determination:²⁶ $R^2 = 1 - SS_e/S_t$, where SS_e =error sum of squares (variance considering regressors), and S_t =total variance (no regressors considered). Pixels with R^2 values < 0.90 were rejected and not considered in calculations or included in saturation maps. The HbSat value of the ROI is reported as the mean HbSat value of the pixels within the ROI. The 95% confidence intervals of the mean HbSat for the ROIs at a single time point were calculated as $\bar{x} \pm z_c(\sigma/\sqrt{n})$, where \bar{x} =ROI mean, z_c =critical value=1.96 for 95% confidence level, σ =ROI standard deviation, and n =number of pixels in the ROI. For statistical analysis, analysis of variance (ANOVA) was performed followed by Newman-Keuls comparison when statistical differences were indicated. A value of $p < 0.05$ was used as the threshold for statistical significance.

For HbSat fluctuation analysis, median ROI HbSat values from 40-min time series were analyzed by examining the power spectra of each time series. Each series of data contained 123 data points sampled at 20-s intervals. In some cases, excessive animal movement or other artifact corrupted the data such that a time point was lost. In this case, linear interpolation was used to fill in the missing data point. No more than two data points in any data set were lost and had to be treated in this manner. To obtain the power spectrum, the data were mean-subtracted to remove the dc component and padded with zeros at the end of the time series to 128 data points (a power of 2) so the fast Fourier transform algorithm could be used for the Fourier transform. Fourier transform of the time series and power spectra were calculated with MATLAB software.

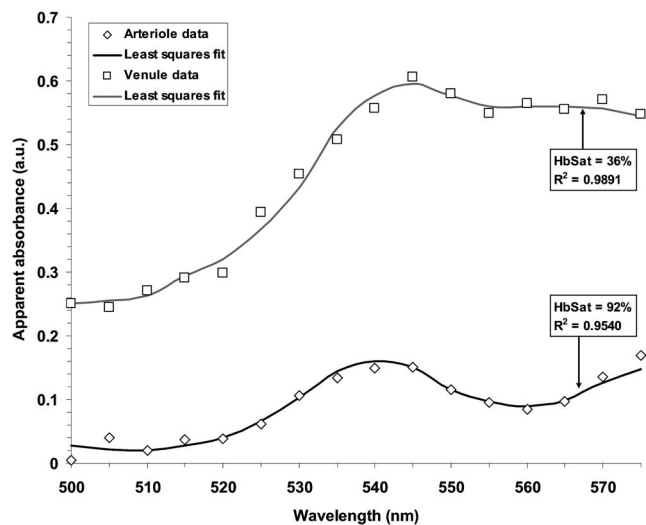


Fig. 1 Example of least-squares fits to pixel spectral data for calculation of HbSat. Each set of data is from an individual pixel in ROI 1 (arteriole) or 2 (venule) in the tumor image from Fig. 10 for the 100% oxygen breathing case.

3 Results

Figure 1 shows examples of HbSat calculations based on linear least-squares fits of the spectral imaging data for individual image pixels. The pixels came from ROIs 1 and 2 in Fig. 10 for the 100% air-breathing condition in the tumor image. Only pixels with $R^2 > 0.90$ were accepted in the creation of the HbSat image maps and calculation of HbSat values in image ROIs; the rest were colored as background in the image maps and omitted from ROI calculations in the figures as detailed previously.²³

3.1 Oxygen Transport Longitudinal Gradients

Figure 2 shows a region of 4T1 tumor microvasculature nine days after tumor cell implantation with various ROIs indicated. The ROIs were chosen such that they followed the

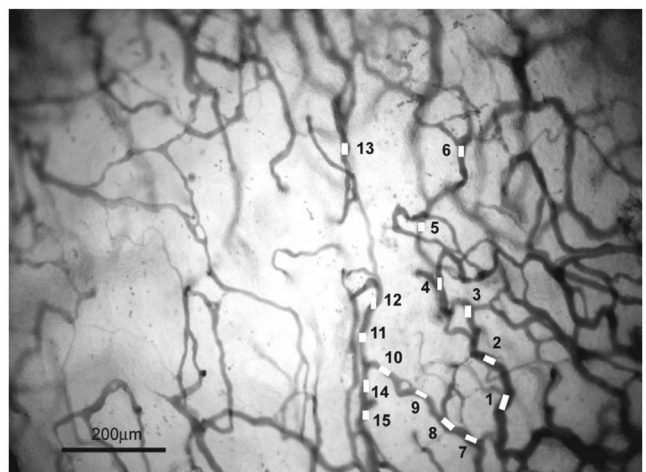


Fig. 2 Tumor nine days after implantation of 5×10^3 cells. The numbered ROIs correspond to the ROIs in Fig. 3 and Table 1. The scale bar is 200 μm (10 \times objective, 0.9 \times 1.2 mm field-of-view).

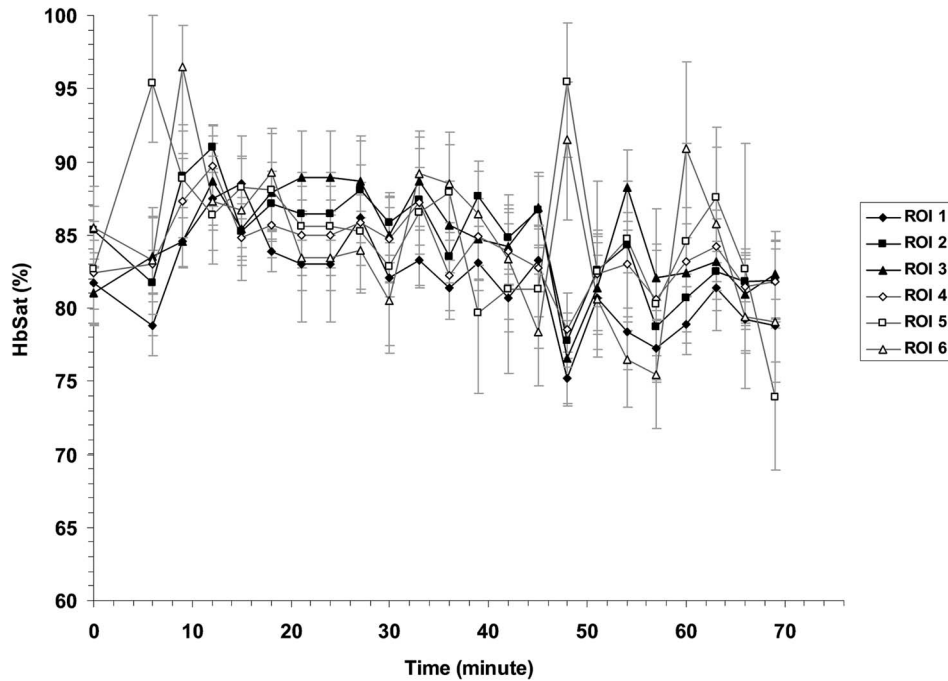


Fig. 3 HbSat fluctuations in ROIs 1 to 6 as indicated in Fig. 2. The data points plotted are the median HbSat \pm interquartile range in the ROI. The lines connecting the data points were added to aid in visualization and do not imply interpolation between time points. Data points were obtained about every 3 min.

course of several microvessels to observe the presence of gradients in HbSat along the vessels. Figure 3 is a graph of the fluctuations recorded at 3-min intervals in HbSat over time for one group of ROIs associated with a particular vessel path. Table 1 is a list of the time-averaged HbSat for each of the ROIs in Fig. 3, with the ROIs grouped by association with a particular vessel path (see Fig. 2). ANOVA and Newman-Keuls comparisons ($p < 0.05$) of the time-averaged HbSat were performed on the separate groups of ROIs (i.e., ROIs 1 to 6, 7 to 10, and 11 to 15). It is evident from Fig. 3 and Table 1 that, for the selected vessels, there is little indication of time-averaged gradients in HbSat. Although for one group of ROIs the difference in the average HbSat of ROI 1 ($82\% \pm 3\%$) from ROIs 2 to 6 rises to the level of statistical significance ($p < 0.05$), biologically this difference is probably not meaningful (maximum average of 85% for ROIs 2 to 6). In ROIs 11 to 15, ROIs 13 and 11, respectively, are statistically the highest ($83\% \pm 3\%$) and lowest ($73\% \pm 5\%$) time-averaged values with the other ROIs somewhere in between and not statistically different from each other. The largest measured fluctuation range in the ROIs for this tumor occurred with ROI 11 (minimum HbSat=55%, maximum HbSat=81%, range=26%). The average fluctuation range of all the ROIs is $18\% \pm 5\%$.

Figure 4 shows a region of 4T1 tumor microvasculature seven days after tumor cell implantation in a tumor different from the one in Fig. 2 with various ROIs chosen similarly as before. A graph of the fluctuations in HbSat over time recorded at 3-min intervals for a group of ROIs is shown in Fig. 5, and Table 2 is a list of the time-averaged HbSat for each of the ROIs in Fig. 4. Statistical comparisons were performed as before. The graph of HbSat temporal fluctuations in Fig. 5 for

Table 1 Time-averaged values of mean HbSat \pm standard deviation for the ROIs in Fig. 2. The ROIs were grouped for statistical analysis (see Sec. 2.4 for details) according to apparent common microvascular flow pathways with groups indicated by horizontal borders in table. Statistically significant differences (ANOVA and Newman-Keuls, $p < 0.05$) are indicated in the table (Y).

ROIs	Time-Averaged HbSat (%) Mean \pm St.Dev.	Statistical Difference $P < 0.05$
ROI 1	82 \pm 3	Y
ROI 2	85 \pm 3	
ROI 3	85 \pm 3	
ROI 4	84 \pm 2	
ROI 5	85 \pm 5	
ROI 6	85 \pm 5	
ROI 7	79 \pm 4	
ROI 8	77 \pm 6	
ROI 9	79 \pm 5	
ROI 10	81 \pm 5	
ROI 11	73 \pm 5	Y
ROI 12	79 \pm 4	
ROI 13	83 \pm 3	Y
ROI 14	78 \pm 5	
ROI 15	80 \pm 4	

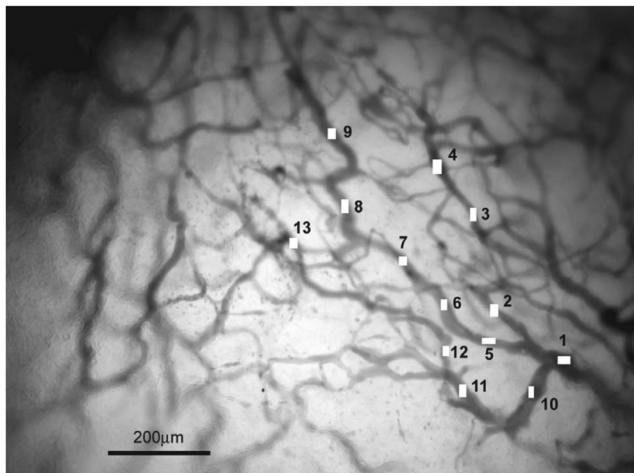


Fig. 4 Tumor seven days after implantation of 5×10^3 cells. The numbered ROIs correspond to the ROIs in Fig. 5 and Table 2. The scale bar is $200 \mu\text{m}$ ($10\times$ objective, 0.9×1.2 mm field-of-view).

the selected group of ROIs clearly shows the presence of gradients in HbSat that persist over time. The time-averaged HbSat values in Table 2 indicate the existence of time-averaged gradients in HbSat in the various groups of ROIs, particularly for ROIs 5 to 9. In this tumor, the fluctuations in HbSat tended to be larger than those for the previously described tumor. The largest measured fluctuation range in the ROIs for the tumor in Fig. 4 occurred with ROI 11 (minimum HbSat=35%, maximum HbSat=83%, range=48%). The average fluctuation range of all the ROIs is $26\% \pm 12\%$. An interesting observation is that within each group of ROIs in this tumor, the ROIs with the highest time-averaged HbSat (ROIs 4, 8, 9, and 13) are all located in close proximity (see Fig. 4), and the average HbSat tends to decrease along each of the respective microvessel branches to-

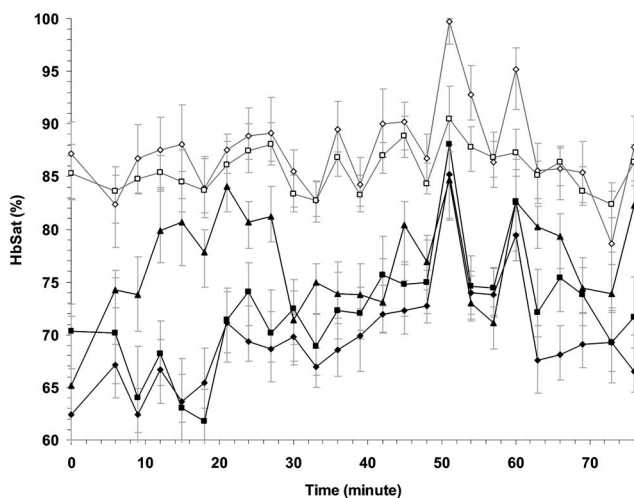


Fig. 5 HbSat fluctuations in ROIs 5 to 9 as indicated in Fig. 4. The data points plotted are the median HbSat \pm interquartile range in the ROI. The lines connecting the data points were added to aid in visualization and do not imply interpolation between time points. Data points were obtained about every 3 min.

Table 2 Time-averaged values of mean HbSat \pm standard deviation for the ROIs in Fig. 4. The ROIs were grouped for statistical analysis (see Sec. 2.4 for details) according to apparent common microvascular flow pathways with groups indicated by horizontal borders in table. Statistically significant differences (ANOVA and Newman-Keuls, $p < 0.05$) are indicated in the table (Y). ROIs 8 and 9 were not statistically different from each other (indicated by "**") but were different from the other ROIs in the analysis group.

ROIs	Time-Averaged HbSat (%) Mean \pm St.Dev.	Statistical Difference $P < 0.05$
ROI 1	74 \pm 4	
ROI 2	72 \pm 6	
ROI 3	81 \pm 5	Y
ROI 4	83 \pm 2	Y
ROI 5	70 \pm 5	Y
ROI 6	72 \pm 5	Y
ROI 7	77 \pm 5	Y
ROI 8	87 \pm 4	Y*
ROI 9	86 \pm 2	Y*
ROI 10	66 \pm 7	
ROI 11	61 \pm 11	
ROI 12	59 \pm 10	
ROI 13	78 \pm 8	Y

ward the junction where they meet (ROI 1), at which point the average HbSat increases. This may imply a common underlying mechanism that affects the general region of the tumor where the observed vessels are located.

In contrast to the tumor microvascular networks, gradients in HbSat such as those found in the tumor were not evident in normal microvessels. Figure 6 shows vessels in a nontumor bearing window chamber two days postsurgery. Next to each ROI in the figure is the 60-min time-averaged HbSat with data points taken at 1-min intervals. With the exception of the ROIs marked with a "*", there was no statistical difference in the average HbSat in this network of vessels (ANOVA and Newman-Keuls, $p < 0.05$) when ROIs were compared to those grouped in the same branch and vessel segment.

3.2 Oxygen Transport Fluctuations

Figure 7 is an example analysis of time series data of HbSat fluctuations. The data in the figure is for a 4T07 tumor at seven days after tumor cell implantation. In Fig. 7(a), the transmitted light image shows a region at the periphery of a tumor, with normal tissue on the left of the image and tumor tissue on the right of the image. ROI 1 is from an arteriole in an area of normal tissue, ROI 2 is from a venule in normal tissue, and ROI 3 is a representative vessel from the tumor microvessel bed seen in the image. Figure 7(b) is a plot of the HbSat fluctuations over time for the three ROIs in Fig. 7(a).

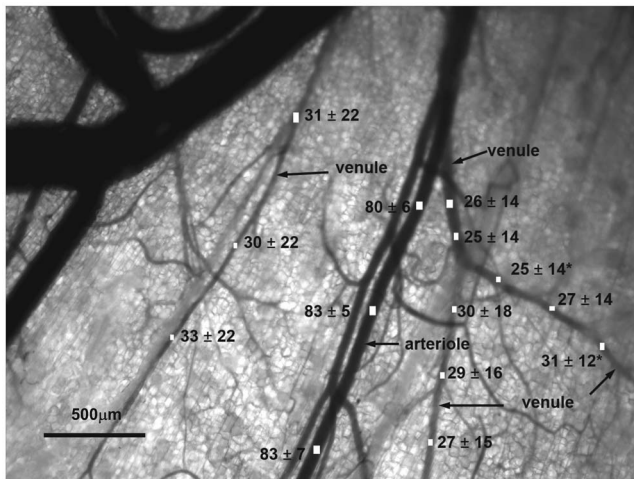


Fig. 6 Image of a normal microvessel network in a nontumor bearing window chamber two days postsurgery ($2.5\times$ objective, 2.2×3.1 mm field-of-view). The mean \pm standard deviation appear next to each ROI along the vessels to indicate the time-averaged HbSat over 60 min. ROIs marked with a "*" were statistically different (ANOVA and Newman-Keuls, $p < 0.05$) when compared to other ROIs along the same vessel segment, but not when compared as a group to other ROIs along the connecting branch segment.

Even though the arteriole HbSat exhibits relatively high frequency HbSat fluctuations, low frequency fluctuations dominate the venule data. The tumor microvessel tends to have an intermediate average HbSat value between the arteriole and venule with low frequency HbSat fluctuations that follow the pattern of the nearby venule. The tumor microvessel fluctuations are larger in magnitude than the venule fluctuations. In Fig. 7(c), it can be seen that a number of higher frequency components are present in the arteriole power spectrum, but lower frequency components dominate the power spectra of the venule and tumor microvessel. This trend was consistent in the 4T1 and 4T07 tumors that were imaged and for normal arterioles and venules in nontumor bearing window chambers. Similar to the spectra in Fig. 7(c), the largest peaks in the power spectra for venules and tumor microvessels occurred for frequencies below 0.2 cpm, and other frequency components generally had less than half the magnitude of the largest peak.

3.3 Anastomosis of Vessels with Different Oxygenations

Figure 8 depicts a direct connection between 4T1 tumor vessels with considerable differences in HbSat. Several smaller vessels with respective saturations of about 66% and 37% converged into one larger diameter vessel. There appeared to be laminar flow in the large diameter vessel, as the different flows propagated without mixing for a distance of at least $500\ \mu\text{m}$. The HbSat and direction of blood flow are indicated in the figure. Figure 9 is another example of this type of connection in a 4T1 tumor. Similar to Fig. 8, several vessels with different HbSats are seen merging together. The saturations of the merging vessels in this example, 61% and 39%, are similar to the values in the previous example in Fig. 8.

Figure 10 is an example of the effect, presumably due to AV anastomoses or similar structures, on oxygen transport in

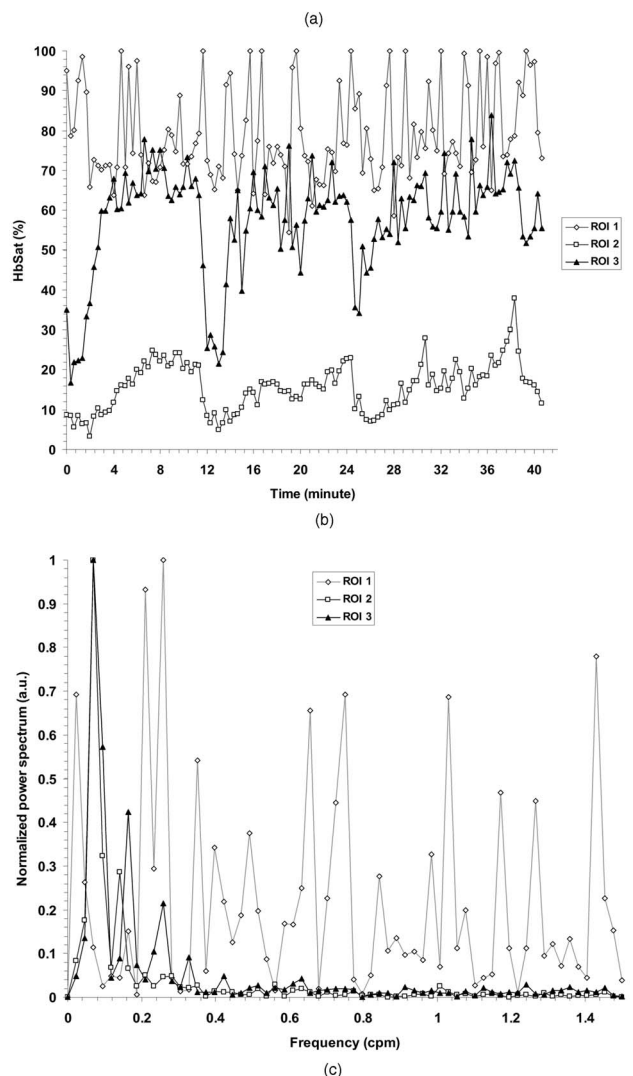
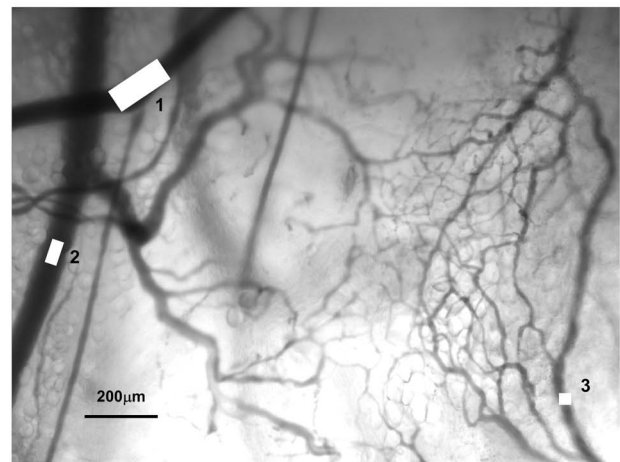


Fig. 7 Fluctuation analysis of HbSat in microvessels. (a) Transmitted light image of the edge of a 4T07 tumor ($5\times$ objective, 1.1×1.6 mm field-of-view). Normal tissue and vessels are on the left side of the image, while tumor tissue and the associated microvessel network are on the right side of the image. ROI 1=normal tissue arteriole, ROI 2=normal tissue venule, ROI 3=tumor microvessel. (b) Temporal fluctuations in HbSat for the ROIs. Data represent median values of a ROI and were acquired at 3 cpm (20-s intervals). Interquartile ranges were omitted for clarity. (c) Normalized power spectra of the time series data for the ROIs.

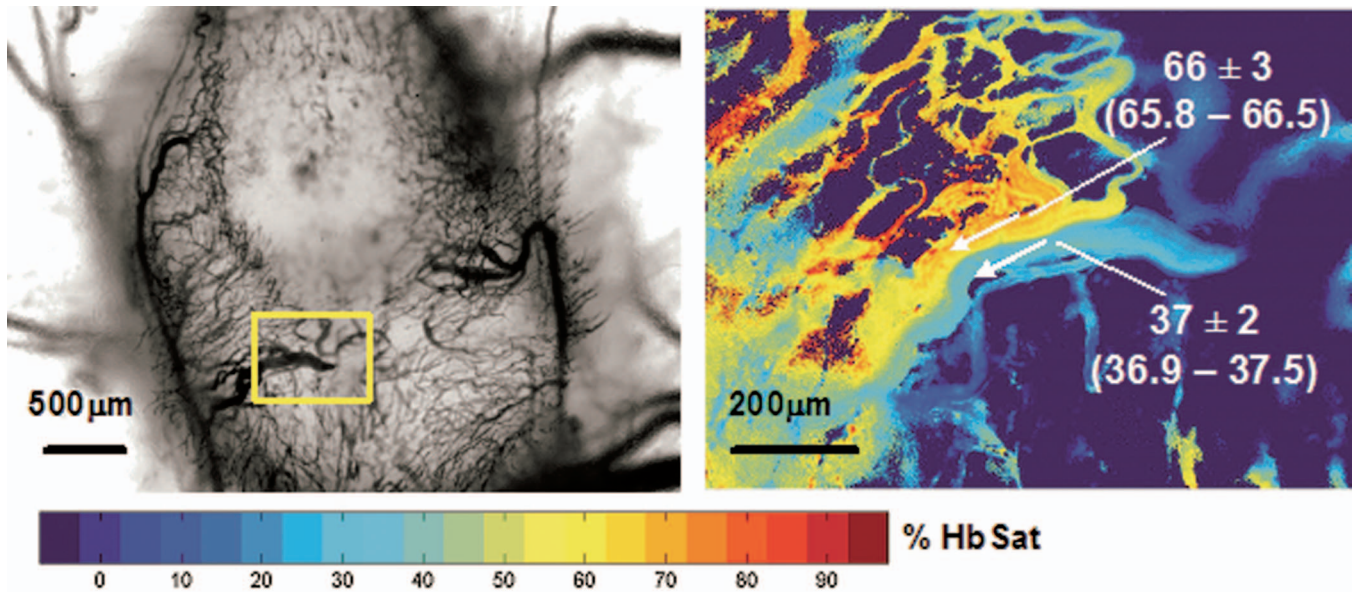


Fig. 8 Images depicting the direct connection of tumor microvessels with highly different HbSats (left=2.5× objective, 3.6×4.8 mm field-of-view; right=10× objective, 0.9×1.2 mm field-of-view). The left image is a low magnification brightfield image, and the right image is a HbSat map of the boxed region in the brightfield image. The direction of blood flow is indicated by the arrows, and the HbSat of the two parallel flows are indicated in the HbSat map. The HbSat values are given as the mean±standard deviation rounded to the nearest percent and 95% confidence intervals for the mean HbSat of the ROI.

a 4T1 tumor nine days after implantation of tumor cells. One set of images shows the tumor, and the other set of images illustrates adjacent normal tissue (some tumor feeding vessels from the tumor images are also visible in the lower right of the normal tissue images). Table 3 contains HbSat values for the ROIs indicated in Fig. 10. Under normal air-breathing conditions, the HbSat in some of the venules immediately adjacent to the tumors (ROIs 4 and 5 in the Fig. 10 tumor) was slightly elevated compared to other nearby venule branches (ROIs 2 and 3 in the Fig. 10 tumor). In the switch to

100% oxygen breathing, there was an appreciable increase in HbSat of almost 30% in the venules that had elevated air-breathing values, which may indicate that some highly oxygenated red blood cells largely bypassed the tumor and were diverted into adjacent venules. Farther away from the tumor in normal tissue, there was no conspicuous indication of this effect in the microvasculature and only a minimal increase in venule HbSat with oxygen breathing. The arterioles in both the tumor (ROI 1) and normal tissue (ROI 2) images in Fig. 10 increased to about the same HbSat with oxygen breathing.

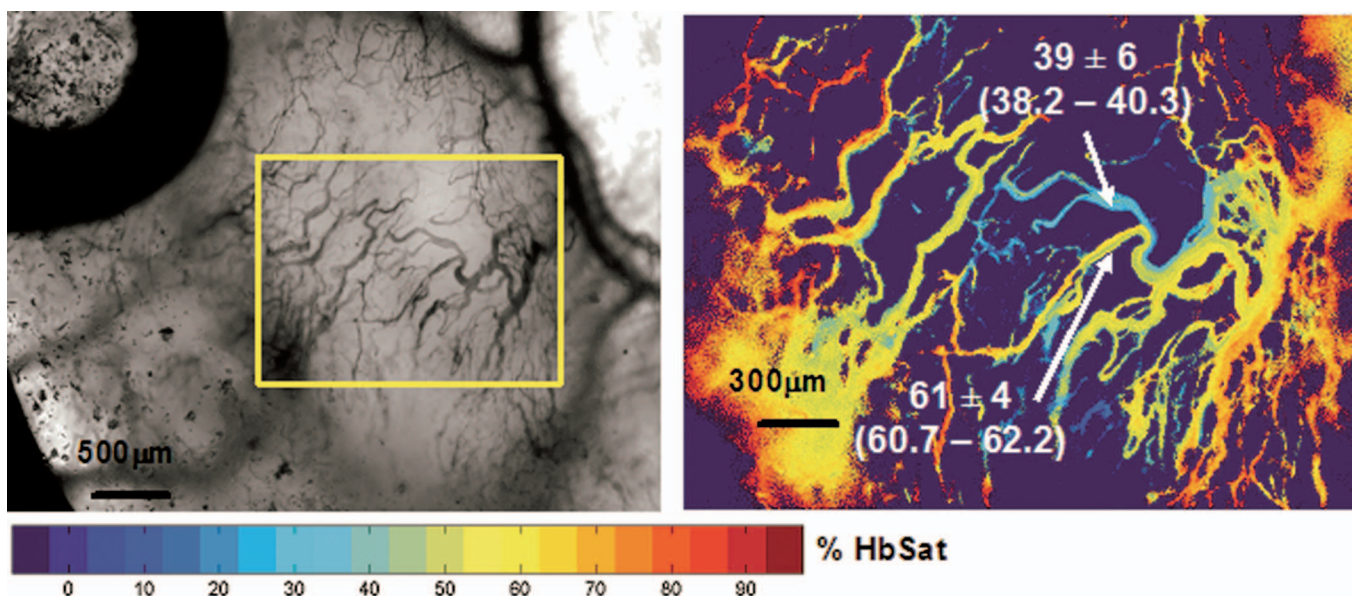


Fig. 9 Another example of merging microvessels with very different HbSat values (left=2.5× objective, 3.6×4.8 mm field-of-view; right=5× objective, 1.8×2.4 mm field-of-view). The HbSat values of the merging vessels are similar to those in Fig. 8. The HbSat values are given as the mean±standard deviation (rounded to the nearest percent) and 95% confidence intervals for the mean HbSat of the ROI.

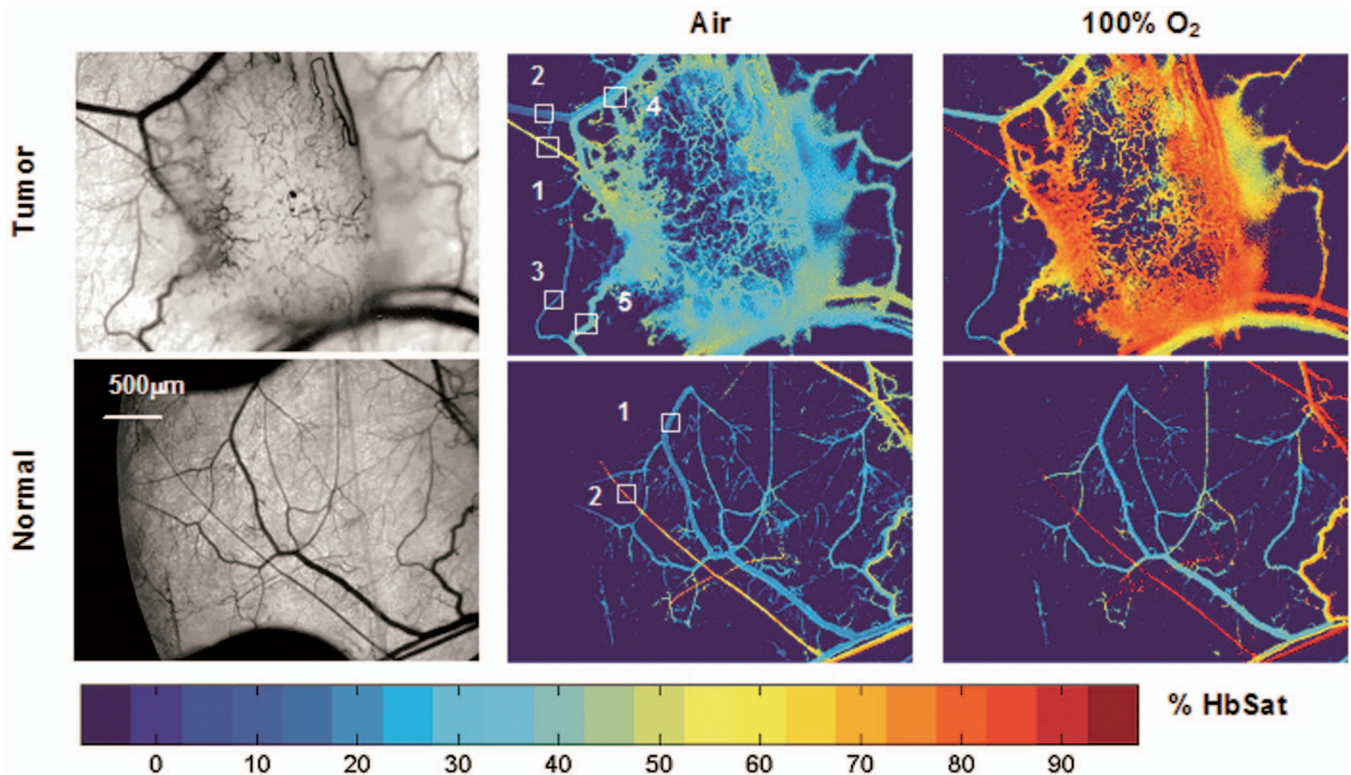


Fig. 10 Effect on tumor oxygen transport believed to be due to AV anastomoses. Switching from air to 100% oxygen breathing raises the HbSat appreciably in tumor associated venule branches, but not in normal tissue venules. The scale bar applies to all of the images ($2.5\times$ objective, 3.6×4.8 mm field-of-view). HbSat values for the ROIs in the figure are given in Table 3.

4 Discussion

We previously described a hyperspectral imaging system for *in vivo* microscopy measurements of tumor microvessel HbSat.²³ An understanding of tumor oxygen transport at the microvascular level is necessary to more fully comprehend the various factors that influence tumor biology, physiology, and therapeutic outcome. For example, longitudinal oxygen gradients of sufficient magnitude to result in chronic intravascular hypoxia have been documented in tumors,¹² demonstrating that patent functional tumor microvessels can still be ineffective at delivering oxygen to some tumor regions. Although individual tumor microvessels are rarely hypoxic, the tissue between the vessels is exquisitely sensitive to the microvessel oxygen concentration. Lanzen et al. recently demonstrated fluctuations in oxygenation of tumor tissue, including fluctuations in the radiobiologic hypoxic range ($pO_2 < 10$ mmHg), that were well correlated to fluctuations in red cell flux of surrounding tumor microvessels.²⁷ The authors also demonstrated how one vessel with a relatively large red cell flux can strongly influence the oxygenation of a region of tumor compared to other nearby vessels. Intermittent hypoxia has emerged as a potentially more important factor than chronic hypoxia in terms of promoting tumor metastasis.¹⁶ Fluctuating tumor oxygenation resulting in intermittent hypoxia-reoxygenation episodes was shown to confer survival and proliferation advantages to both tumor and endothelial cells at a molecular level via hypoxia-inducible factor-1 α (HIF-1 α) mediated pathways.¹⁵ Slow fluctuations in pO_2 documented in spontaneous canine tumors increase the likelihood that such effects also occur in human tumors.²⁸

Taken together, this knowledge indicates that HIF-1 α is an important target to be considered for drug development to ameliorate the negative effects of fluctuating oxygenation on tumor progression and treatment.¹⁴ In another example, a recent review of the tumor oxygenation effects of a variety of

Table 3 HbSat values for the ROIs indicated in Fig. 10. The ROIs are indicated in the middle group of images (“Air”). The HbSat values are given as the Mean \pm standard deviation (rounded to the nearest percent) and 95% confidence intervals for the means HbSat of the ROI.

Region	HbSat(%)	
	Air	100% O ₂
Tumor		
1	56 \pm 5 (55.2 to 56.8)	93 \pm 5 (91.9 to 94.1)
2	16 \pm 3 (15.7 to 16.3)	35 \pm 3 (35.6 to 36.6)
3	24 \pm 8 (22.6 to 25.0)	28 \pm 6 (26.8 to 29.9)
4	32 \pm 4 (31.2 to 33.2)	61 \pm 6 (59.7 to 61.7)
5	35 \pm 5 (34.2 to 35.3)	67 \pm 4 (66.1 to 67.6)
Normal		
1	22 \pm 4 (20.8 to 22.2)	27 \pm 3 (27.5 to 29.0)
2	76 \pm 7 (75.9 to 78.5)	95 \pm 6 (93.5 to 96.2)

angiogenesis-inhibiting agents (AIAs) revealed mixed results—increases, decreases, and no changes were documented—thus the mechanisms involved in alterations of tumor oxygenation by AIAs are at present not fully understood.²⁹ Knowledge of the oxygenation effects of AIAs is important so that they can be rationally combined with other conventional therapies for maximum effect, particularly for radiation therapy.²⁹

In this paper, we demonstrate spectral imaging measurements of HbSat fluctuations and spatial gradients in 4T1 and 4T07 mouse mammary adenocarcinomas. The data in Figs. 2–5 illustrate differences in oxygen transport in tumor microvascular networks that can occur between individual tumors. In the tumor in Fig. 2, there were relatively few longitudinal gradients that persisted over time. The average fluctuations in HbSat that occurred were generally consistent between the ROIs (standard deviation of 5%). In contrast, the tumor in Fig. 4 had more examples of chronic longitudinal gradients; the fluctuations in HbSat on average were larger than in the tumor in Fig. 2; and there was greater variation in the range of fluctuations between the ROIs (standard deviation of 12%). The HbSat longitudinal gradients observed in the tumor microvessel branches were not observed in normal vessel branches as in Fig. 6. Duling documented longitudinal gradients in a hamster cheek pouch normal microvascular network along network vessels with HbSat values (calculated from microelectrode pO_2 measurements) of 70% at an artery to about 33% at a precapillary arteriole.³⁰ Assuming a linear gradient in HbSat, then a rough estimation of the gradient in the networks measured by Duling (represented in Fig. 3 from Ref. 30) was minimally $0.0019\%/\mu\text{m}$ and maximally $0.012\%/\mu\text{m}$. In contrast, for the tumor in Fig. 4 in this study for ROIs 5 to 9, the gradient in HbSat is roughly $0.033\%/\mu\text{m}$, or 2.75 to 17 times greater than that measured by Duling. This contrast may reflect differences in tissue type, such as normal versus tumor microvessels, or animal model, such as mouse skin versus hamster cheek pouch. It should also be noted that in the network measured by Duling, the longitudinal gradients occurred along several different branching orders of vessels, but in the tumor data presented here, the observed gradients occurred along what appeared to be a single vessel segment, albeit a tortuous, highly branched, and abnormal one. Imaging on consecutive days is required to see if these characteristics are relatively stable for a particular tumor or if they change over time as the tumor develops.

Data acquisition at higher temporal resolution revealed slow fluctuations in HbSat in tumor microvessels. As seen in Fig. 7, these fluctuations were similar to those in normal venules, but the arteriole data showed high magnitude fluctuations with relatively high frequency. The magnitude of the fluctuations in the tumor microvessels was sometimes larger than in normal venules. Braun et al. postulate that a number of different mechanisms, including arteriolar vasomotion, blood flow changes induced by hemodynamic phenomena, and intussusceptive microvessel growth, may be responsible for observed fluctuations in tumor pO_2 measured with oxygen microelectrodes.¹³ The measured slow temporal fluctuations (≤ 0.2 cpm) in tumor microvessel HbSat were consistent with microelectrode measurements of pO_2 fluctuations in rat mammary adenocarcinoma, fibrosarcoma, and glioma tumors

(0.12 to 0.28 cpm),^{13,31} and spontaneous canine tumors (≤ 0.003 Hz or 0.18 cpm).²⁸ Our preliminary data suggest that at least in some tumor microvessels, mechanisms that are responsible for fluctuations in normal venule HbSat may contribute to fluctuations in tumor microvessel HbSat and hence to tumor pO_2 fluctuations.

There was significant vasomotion in the arterioles observed during imaging. Arteriole vasomotion in the frequency range of 0.4 to 15 cpm has been documented previously.^{32,33} It is possible that the arteriole data contains artifacts due to vasomotion and the fact that accurate sampling of frequencies higher than 1.5 cpm are beyond the frequency resolution of the imaging system (3-cpm sampling rate results in a Nyquist frequency of 1.5 cpm), thus there may be aliasing of higher frequency components represented as artifacts in frequencies below 1.5 cpm in our data. It should be noted that due to the geometry of the window chamber, tumors had unrestricted growth on the side of the chamber without a coverslip and thus would bulge out at some point during growth. Thus, the vessels that were imaged at later time points were generally on the tumor periphery. These vessels are general relatively well oxygenated compared to vessels located deeper in the tumor. However, vessels that emerge from deeper in the tissue to the surface (periphery) are also sometimes seen, and these vessels generally have lower saturation on the order of 30% or less. This may explain why the venules from normal tissue in Fig. 6 have lower saturations than the tumor vessels in Figs. 3 and 5.

In Figs. 8 and 9, we visualized the convergence and direct connection of tumor microvessels with diameters $\leq 100 \mu\text{m}$ and HbSats that differed by more than 20%. As both of the merging vessels are venules, the difference in oxygenation may be explained in part by the different paths taken by the vessels through the tumor tissue. In Fig. 8, for example, the less oxygenated vessel emerges from deeper tumor tissue but the more oxygenated vessel traverses a more superficial path. The merging of vessels like this will undoubtedly affect the flow dynamics within the local network due to differences in the mechanical properties of the red blood cells (less oxygenated red blood cells are less deformable than well oxygenated ones³⁴).

During the process of angiogenesis and neovascularization, sprouts arising from venules can anastomose with neighboring arterioles. In some instances, tumor vascular networks can be both supplied and drained by venules due to AV anastomoses.¹⁹ AV anastomoses in tumors may adversely impact various therapeutic modalities, including chemo-, radio-, and immunotherapies, by providing an alternate route for blood flow that bypasses tumor tissue.³⁵ Angiography studies, such as those by Lagergren in human fibrosarcomas, demonstrated shunting of contrast medium from the arterial to venous side of a tumor microvascular network, highlighting the presence of AV anastomoses.³⁶ Warren details work that showed an increase in the oxygen content of venous blood existing tumors, presumably due to AV shunts.³⁷ Mariani et al. demonstrated intratumoral shunting of arterially injected radio-labeled particles from malignant gliomas to the lungs.³⁸ In Fig. 10, venules immediately adjacent to a tumor showed what appeared to be a diversion of highly oxygenated red blood cells around the tumor upon a switch from air to 100%

oxygen breathing, presumably due to AV anastomoses or equivalent structures within the tumor. This phenomenon was not observed in venules further removed from the tumor. Several methods have been studied preclinically and clinically to ameliorate tumor hypoxia by increasing microvascular oxygen content; however, those based on hyperoxic gas breathing at ambient and hyperbaric pressures have had very limited success.^{39,40} A number of factors have been implicated for the failure of hyperoxic gas breathing to significantly improve radiotherapeutic outcome, including longitudinal pO₂ gradients, abnormal tumor microvascular geometry, inadequate oxygen delivery relative to tumor demands, and unstable blood flow due to vasoactive effects.⁴¹ The diversion of oxygenated blood to tumor draining venules, as demonstrated in this study, may be another mechanism that limited the success of previous hyperoxic gas breathing trials.

5 Conclusion

Recent publications have demonstrated the utility of spectral imaging for measurements of HbSat in networks of microvessels.^{23,42} In this paper, we have demonstrated that spectral imaging of tumor microvasculature can be used for measurements of oxygen transport parameters with relevance to current questions about tumor biology and treatment outcome. In future studies, we plan to employ this technique to study tumor oxygen transport effects of vascular-targeting drugs.

Acknowledgments

Funding for this project was provided in part by National Institutes of Health Grants Nos. R01 CA 40355 (NCI), P50 CA 068438 (NCI), and T32 EB01630 (NIBIB).

References

1. T. M. Busch, E. P. Wileyto, S. M. Evans, and C. J. Koch, "Quantitative spatial analysis of hypoxia and vascular perfusion in tumor sections," *Adv. Exp. Med. Biol.* **510**, 37–43 (2003).
2. D. J. Chaplin, M. R. Horsman, M. J. Trotter, and D. W. Siemann, "Therapeutic significance of microenvironmental factors," in *Blood Perfusion and Microenvironment of Human Tumors*, M. Molls and P. Vaupel, Eds., pp. 133–143, Springer-Verlag, New York (1998).
3. M. W. Dewhirst, "Concepts of oxygen transport at the microcirculatory level," *Semin. Radiat. Oncol.* **8**, 143–150 (1998).
4. R. E. Durand and N. E. LePard, "Contribution of transient blood flow to tumor hypoxia in mice," *Acta Oncol.* **34**, 317–323 (1995).
5. R. K. Jain, "Normalizing tumor vasculature with anti-angiogenic therapy: A new paradigm for combination therapy," *Nat. Med.* **7**, 987–989 (2001).
6. P. Vaupel, A. Mayer, S. Briest, and M. Höckel, "Hypoxia in breast cancer: Role of blood flow, oxygen diffusion distances, and anemia in the development of oxygen depletion," *Adv. Exp. Med. Biol.* **566**, 333–342 (2005).
7. M. R. Horsman and J. Overgaard, "The oxygen effect," in *Basic Clinical Radiobiology*, 2nd ed., G. G. Steel, Ed., pp. 132–140, Oxford University Press, New York (1997).
8. A. M. Shannon, D. J. Bouchier-Hayes, C. M. Condrón, and D. Toomey, "Tumor hypoxia, chemotherapeutic resistance and hypoxia-related therapies," *Cancer Treat Rev.* **29**, 297–307 (2003).
9. A. L. Harris, "Hypoxia—a key regulatory factor in tumor growth," *Nat. Rev. Cancer* **2**, 38–47 (2001).
10. M. Höckel and P. Vaupel, "Tumor hypoxia: Definitions and current clinical, biologic, and molecular aspects," *J. Natl. Cancer Inst.* **93**, 266–276 (2001).
11. H. Kimura, R. D. Braun, E. T. Ong, R. Hsu, T. W. Secomb, D. Papahadjopoulos, K. Hong, and M. W. Dewhirst, "Fluctuations in red cell flux in tumor microvessels can lead to transient hypoxia and reoxygenation in tumor parenchyma," *Cancer Res.* **56**, 5522–5528 (1996).
12. M. W. Dewhirst, E. T. Ong, R. D. Braun, B. Smith, B. Klitzman, S. M. Evans, and D. Wilson, "Quantification of longitudinal tissue pO₂ gradients in window chamber tumours: Impact on tumour hypoxia," *Br. J. Cancer* **79**, 1717–1722 (1999).
13. R. D. Braun, J. L. Lanzen, and M. W. Dewhirst, "Fourier analysis of fluctuations of oxygen tension and blood flow in R3230Ac tumors and muscle in rats," *Am. J. Physiol.* **277**, H551–H568 (1999).
14. M. W. Dewhirst, "Intermittent hypoxia furthers the rationale for hypoxia-inducible factor-1 targeting," *Cancer Res.* **67**, 854–855 (2007).
15. P. Martinive, F. Defresne, C. Bouzin, J. Saliez, F. Lair, V. Grégoire, C. Michiels, C. Dessy, and O. Feron, "Preconditioning of the tumor vasculature and tumor cells by intermittent hypoxia: Implications for anticancer therapies," *Cancer Res.* **66**, 11736–11744 (2006).
16. E. K. Rofstad, K. Galappathi, B. Mathiesen, and E.-B. M. Ruud, "Fluctuating and diffusion-limited hypoxia in hypoxia-induced metastasis," *Clin. Cancer Res.* **13**, 1971–1978 (2007).
17. A. Zakrzewicz, T. W. Secomb, and A. R. Pries, "Angioadaptation: Keeping the vascular system in shape," *News Physiol. Sci.* **17**, 197–201 (2002).
18. R. K. Jain, "Determinants of tumor blood flow: A review," *Cancer Res.* **48**, 2641–2658 (1988).
19. P. Vaupel, F. Kallinowski, and P. Okunieff, "Blood flow, oxygen and nutrient supply, and metabolic microenvironment of human tumors: A review," *Cancer Res.* **49**, 6449–6465 (1989).
20. D. W. Siemann, "The tumor microenvironment: A double-edged sword," *Int. J. Radiat. Oncol., Biol., Phys.* **42**, 697–699 (1998).
21. S. Ho, W. Y. Lau, W. T. Leung, M. Chan, K. W. Chan, P. J. Johnson, and A. K. C. Li, "Arteriovenous shunts in patients with hepatic tumors," *J. Nucl. Med.* **38**, 1201–1205 (1997).
22. S. R. McDougall, A. R. A. Anderson, M. A. J. Chaplain, and J. A. Sheratt, "Mathematical modelling of flow through vascular networks: Implications for tumor-induced angiogenesis and chemotherapy strategies," *Bull. Math. Biol.* **64**, 673–702 (2002).
23. B. S. Sorg, B. J. Moeller, O. Donovan, Y. Cao, and M. W. Dewhirst, "Hyperspectral imaging of hemoglobin saturation in tumor microvasculature and tumor hypoxia development," *J. Biomed. Opt.* **10**, 044004 (2005).
24. B. S. Sorg, B. J. Moeller, O. Donovan, Y. Cao, and M. W. Dewhirst, "Measurement of hemoglobin saturation in tumor microvasculature in preclinical models using hyperspectral imaging," *Proc. SPIE* **5694**, 74–81 (2005).
25. R. D. Shonat, E. S. Wachman, W.-H. Niu, A. P. Koretsky, and D. L. Farkas, "Near-simultaneous hemoglobin saturation and oxygen tension maps in mouse brain using an AOTF microscope," *Biophys. J.* **73**, 1223–1231 (1997).
26. D. C. Montgomery and E. A. Peck, *Introduction to Linear Regression Analysis*, Wiley-Liss, New York (1992).
27. J. Lanzen, R. D. Braun, B. Klitzman, D. Brizel, T. W. Secomb, and M. W. Dewhirst, "Direct demonstration of instabilities in oxygen concentrations within the extravascular compartment of an experimental tumor," *Cancer Res.* **66**, 2219–2223 (2006).
28. K. G. Brurberg, H. K. Skogmo, B. A. Graff, D. R. Olsen, and E. K. Rofstad, "Fluctuations in pO₂ in poorly and well-oxygenated spontaneous canine tumors before and during fractionated radiation therapy," *Radiat. Oncol.* **77**, 220–226 (2005).
29. M. R. Horsman and D. W. Siemann, "Pathophysiologic effects of vascular-targeting agents and the implications for combination with conventional therapies," *Cancer Res.* **24**, 11520–11539 (2006).
30. B. R. Duling and R. M. Berne, "Longitudinal gradients in periarterial oxygen tension," *Circ. Res.* **27**, 669–678 (1970).
31. L. I. Cardenas-Navia, D. Yu, R. D. Braun, D. M. Brizel, T. W. Secomb, and M. W. Dewhirst, "Tumor-dependent kinetics of partial pressure of oxygen fluctuations during air and oxygen breathing," *Cancer Res.* **64**, 6010–6017 (2004).
32. A. Colantuoni, S. Bertuglia, and M. Intaglietta, "Quantitation of rhythmic diameter changes in arterial microcirculation," *Am. J. Physiol.* **246**, H508–H517 (1984).

33. W. G. Hundley, G. J. Renaldo, J. E. Levasseur, and H. A. Kontos, "Vasomotion in cerebral microcirculation of awake rabbits," *Am. J. Physiol.* **254**, H67–H71 (1988).
34. B. D. Kavanagh, B. E. Coffey, D. Needham, R. M. Hochmuth, and M. W. Dewhirst, "The effect of flunarizine on erythrocyte suspension viscosity under conditions of extreme hypoxia, low pH, and lactate treatment," *Br. J. Cancer* **67**, 734–741 (1993).
35. P. Vaupel, "Tumor blood flow," in *Blood Perfusion and Microenvironment of Human Tumors*, M. Molls and P. Vaupel, Eds., pp. 41–45, Springer-Verlag, Berlin (1998).
36. C. Lagergren, Å. Lindbom, and G. Söderberg, "Vascularization of fibromatous and fibrosarcomatous tumors," *Acta Radiol. (1921-1962)* **53**, 1–16 (1960).
37. B. A. Warren, "The vascular morphology of tumors," in *Tumor Blood Circulation: Angiogenesis, Vascular Morphology and Blood Flow of Experimental and Human Tumors*, H.-I. Peterson, Ed., pp. 1–47, CRC Press, Inc., Boca Raton, Fla. (1979).
38. L. Mariani, G. Schroth, J. P. Wielepp, A. Haldemann, and R. W. Seiler, "Intratumoral arteriovenous shunting in malignant gliomas," *Neurosurgery* **48**, 353–358 (2001).
39. D. W. Siemann, M. R. Horsman, and D. J. Chaplin, "Modification of oxygen supply," in *Blood Perfusion and Microenvironment of Human Tumors*, M. Molls and P. Vaupel, Eds., pp. 209–217, Springer-Verlag, Berlin (1998).
40. P. Vaupel, D. K. Kelleher, and O. Thews, "Modulation of tumor oxygen," *Int. J. Radiat. Oncol., Biol., Phys.* **42**, 843–848 (1998).
41. J. L. Lanzen, R. D. Braun, A. L. Ong, and M. W. Dewhirst, "Variability in blood flow and pO₂ in tumors in response to carbogen breathing," *Int. J. Radiat. Oncol., Biol., Phys.* **42**, 855–859 (1998).
42. B. Styp-Rekowska, N. M. Disassa, B. Reglin, L. Ulm, H. Kuppe, T. W. Secomb, and A. R. Pries, "An imaging spectroscopy approach for measurement of oxygen saturation and hematocrit during intravital microscopy," *Microcirculation (Philadelphia)* **14**, 207–221 (2007).